Research on Hypersonic Boundary-Layer Stability with High-Temperature Effects

Xianliang Chen[1], Pietro Carlo Boldini[2], and Song Fu[1(✉)]

[1] Tsinghua University, Beijing 100084, China
fs-dem@tsinghua.edu.cn
[2] Institute of Aerodynamics and Gas Dynamics, University of Stuttgart, 70550 Stuttgart, Germany

Abstract. High-temperature effects need to be considered for a better design of hypersonic and reentry vehicles. They affect both the boundary layer flow and its flow transition, whose primary stages can be investigated through modal stability analysis. In this work, physical and numerical tools for high-temperature flows are presented and the efficiency of the new developed in-house boundary layer and stability solvers is tested. Specially, we focus on the stability of a flat plate flow in thermochemical non-equilibrium through an investigation of growth rates under the influence of various flow parameters.

Keywords: Hypersonic flow · Modal instability · High-temperature effects

1 Introduction

Transition of hypersonic boundary layers from laminar to turbulence is crucial for the high-speed vehicle design. Transition is reported to increase the surface heating loads by a factor of 4–10 [18], thus the accurately-predicted aerodynamic design can greatly decrease the requirement for the Thermal Protection System and improve flight efficiency. However, the transition phenomenon is extremely complicated, as it can be strongly dependent on environmental conditions and boundary conditions. Morkovin [1] gave five different paths of transition according to the magnitude of the environmental disturbances. Low level of external disturbances relates to the Natural Transition process, which is applicable for high altitude atmospheric environment. This paper will focus on the modal growth process that natural transition needs to undergo under the framework of Linear Stability Theory (LST) [2].

On the other hand, an important feature of hypersonic flow is the steeply rising temperature as the Mach number increases. Taking the Apollo reentry as an example, the flight speed of Mach 36 will give a post-shock temperature of more than 50000 K under the assumption of a calorically perfect gas (CPG), while the actual temperature is about 11000 K [3]. The huge difference is due to the so-called high-temperature effect, where an extremely high gas temperature excites the vibrational energy of air molecules and causes chemical dissociation or even ionization, resulting in the failure of the calorically perfect gas assumption. Since the thermo-chemical equilibrium cannot be physically reached everywhere, in order to describe the thermo-chemical non-equilibrium (TCNEQ) process, additional equations are needed to describe the

X. Zhang (Ed.): APISAT 2018, LNEE 459, pp. 499–512, 2019.
https://doi.org/10.1007/978-981-13-3305-7_41

convection and diffusion of vibrational energy, electronic energy and component mass [4]. The high-temperature effect will inevitably affect the basic flow, as well as stability and transition process in the flow field.

Malik [5] pioneered the research of the real gas effects on the stability of boundary layers. Stuckert [6], Hudson [7], Klentzman [8] and Miró [19] used LST to analyze the effects of thermo-chemical processes, but these works focused on the instability modes instead of the evolution of discrete modes. The new framework of boundary layer stability proposed by Fedorov and Tumin [9] provides an insight of the evolution and interaction between modes. On this basis, Bitter and Sherpherd [18] analyzed the thermal non-equilibrium boundary layer with extremely cooled wall, but the results are mainly around Mach 5, without considering higher Mach numbers and chemical processes. In summary, the objective of this paper is to study the effects of thermo-chemical non-equilibrium process on the stability of high-speed boundary layers, especially the evolution and interaction of discrete modes.

2 Governing Equations and Physical Models

2.1 Navier-Stokes Equations

We consider a 5-species model (N_2, O_2, NO, N, O) without ionization. Introducing the Two-Temperature Model proposed by Park [12], we arrive at the NS equations for the thermo-chemical non-equilibrium flow as Eqs. 1–5:

Continuity Equation:

$$\frac{\partial \rho^*}{\partial t^*} + \nabla^* \cdot (\rho^* \boldsymbol{u}^*) = 0 \tag{1}$$

Momentum Equation:

$$\rho^* \frac{\mathrm{D}\boldsymbol{u}^*}{\mathrm{D}t^*} = -\nabla^* P^* + \nabla^* \cdot \left[\mu^* \left(\nabla^* \boldsymbol{u}^* + \nabla^* \boldsymbol{u}^{*\mathrm{T}}\right)\right] + \nabla^* \left[\lambda^* \nabla^* \cdot \boldsymbol{u}^*\right] \tag{2}$$

Energy Equation:

$$\rho^* c_p^* \frac{\mathrm{D}T^*}{\mathrm{D}t^*} - \frac{\mathrm{D}P^*}{\mathrm{D}t^*} = \nabla^* \cdot (k^* \nabla^* T^*) + \boldsymbol{\Phi}^* + \left(\sum_m \rho^* D_m^* c_{p,m}^* \nabla Y_m\right) \cdot \nabla T^* - \left(h_m^* \dot{\omega}_m^* + Q_{t-v}^*\right) \tag{3}$$

Vibrational Energy Equation:

$$\rho^* c_{vib}^* \frac{\mathrm{D}T_{vib}^*}{\mathrm{D}t^*} - \frac{\mathrm{D}P^*}{\mathrm{D}t^*} = \nabla^* \cdot \left(k_{vib}^* \nabla^* T_{vib}^*\right) + \left(\sum_m \rho^* D_m^* c_{vib,m}^* \nabla Y_m\right) \cdot \nabla T_{vib}^* + Q_{t-v}^* \tag{4}$$

Species Equation:

$$\rho^* \frac{\mathrm{D}Y_s}{\mathrm{D}t^*} = \nabla^* \cdot \left(\rho^* D_s^* \nabla^* Y_s\right) + \dot{\omega}_s^* \tag{5}$$

Here asterisk denotes dimensional quantities; Y_s is the species mass fraction with $s \in [2, \cdots, n_s]$ the species index; c_p^* is the heat capacity at constant pressure, c_{vib}^* is the vibrational heat capacity and h_m^* is the species enthalpy; k_{vib}^* is the vibrational thermal conductivity, D_s^* is the coefficient of species mass diffusion; $\mathbf{\Phi}^*$ is the viscous dissipation function, Q_{t-v}^* and $\dot{\omega}_s$ are the source terms for thermal (TNEQ) and chemical non-equilibrium (CNEQ).

2.2 Non-equilibrium Models

The vibrational energy is calculated from kinetic theory as:

$$e_{vib,s}^*\left(T_{vib}^*\right) = \frac{\theta_{vib,s}^* R_s^*}{\exp\left(\frac{\theta_{vib,s}^*}{T_{vib}^*}\right) - 1}$$

where $\theta_{vib,s}^*$ is the characteristic vibrational temperature. As for the non-equilibrium case, the Landau-Teller equation is introduced to describe the energy exchange and relaxation:

$$Q_{t-v}^* = \sum_{s=1}^{n_v} \rho_s^* \frac{e_{vib,s}^*(T^*) - e_{vib,s}^*\left(T_{vib}^*\right)}{\tau_s^*}$$

where the relaxation time is based on Millikan and White's [10] semi-empirical curve fits.

The chemical source term is based on the finite-rate reacting model:

$$\dot{\omega}_s^* = M_s \sum_{r=1}^{n_r} \left(v_s'' - v_s'\right) \left\{ k_{f,rs} \prod_i c_i^{v_i'} - k_{b,rs} \prod_i c_i^{v_i''} \right\}$$

Here five specific reactions are considered:

$$R_1\text{: } \mathrm{N_2} + M \leftrightarrow 2\mathrm{N} + M$$

$$R_2\text{: } \mathrm{O_2} + M \leftrightarrow 2\mathrm{O} + M$$

$$R_3\text{: } \mathrm{NO} + M \leftrightarrow \mathrm{N} + \mathrm{O} + M$$

$$R_4\text{: } \mathrm{N_2} + \mathrm{O} \leftrightarrow \mathrm{NO} + \mathrm{N}$$

$$R_5\text{: } \mathrm{NO} + \mathrm{O} \leftrightarrow \mathrm{O_2} + \mathrm{N}$$

Details can be found in Park [11].

For the viscous coefficient, Wilke's rule [13] is employed to treat the mixture. Species viscosity is obtained from Blottner [14] and thermal conductivities are calculated from Eucken's relation [15]. A constant Schmidt number is assumed for the mass diffusion coefficient [7]. The wall boundary is no-slip, adiabatic/isothermal and non-catalytic.

2.3 Calculation of Basic Flow

A precise and efficient basic flow solver is needed for the stability analysis. One can directly solve the NS equations using either shock capture [7] or shock fitting [16] methods to obtain a reliable basic flow, while we turn to boundary layer equations here to realize a more time-saving solver. With knowledge of the self-similar solution of CPG, we apply the non-dimensional Lees-Dorodnitsyn transformation:

$$\begin{cases} \xi(x,y) = x \\ \eta(x,y) = \sqrt{\frac{Re_L}{x}} \int_0^y \rho \mathrm{d}y \end{cases}$$

For a flat plate, the transformed equation is generally written as:

$$\frac{\partial^2 \phi}{\partial \eta^2} + \frac{\partial C}{\partial \eta}\frac{\partial \phi}{\partial \eta} = \xi\left(\phi \frac{\partial \phi}{\partial \xi} + S\right)$$

where $\varphi = [\mathrm{U}, \mathrm{T}, \mathrm{T_{vib}}, \mathrm{Y_s}]^{\mathrm{T}}$ separately and S is the non-equilibrium source term. Due to the existence of source terms, the self-similar solution is no longer available. Fortunately, we notice that when $\xi = 0$, the equation is ordinary again. Making use of the parabolic nature, one can march in the stream-wise direction from $\xi = 0$. We use 4-th order finite differences in the ξ direction and spectral method with Chebyshev interpolation points in the η direction. The solution is updated using Newtonian iteration.

Validation of the base flow solver is performed with a comparison to the latest literature sources available. The in-house base flow solver has been verified against two different kind of flows, a TNEQ and CNEQ case.

- TNEQ case in [18]: The high-temperature flat plate flow is investigated. Air is modeled as mixture of 78% N_2 and 22% O_2. The flow is in thermal nonequilibrium with a Mach number of 5 and free stream pressure of 20 kPa. The free stream temperature is set to 1500 K and isothermal wall at 300 K is prescribed.
  The dimensional velocity and temperature profiles are extracted at $\mathrm{Re_x} = 1500$. The results are plotted in Fig. 1 and show good agreement with the boundary layer solutions of Bitter [18].

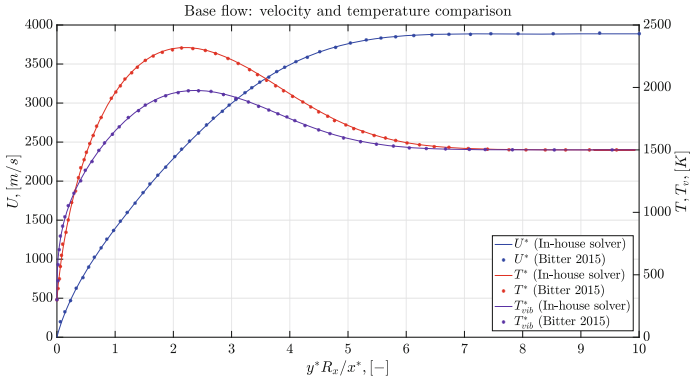

Fig. 1. Dimensional velocity and temperature profile over the dimensionless wall normal coordinate: comparison between the in-house base flow solver and Bitter's results [18]

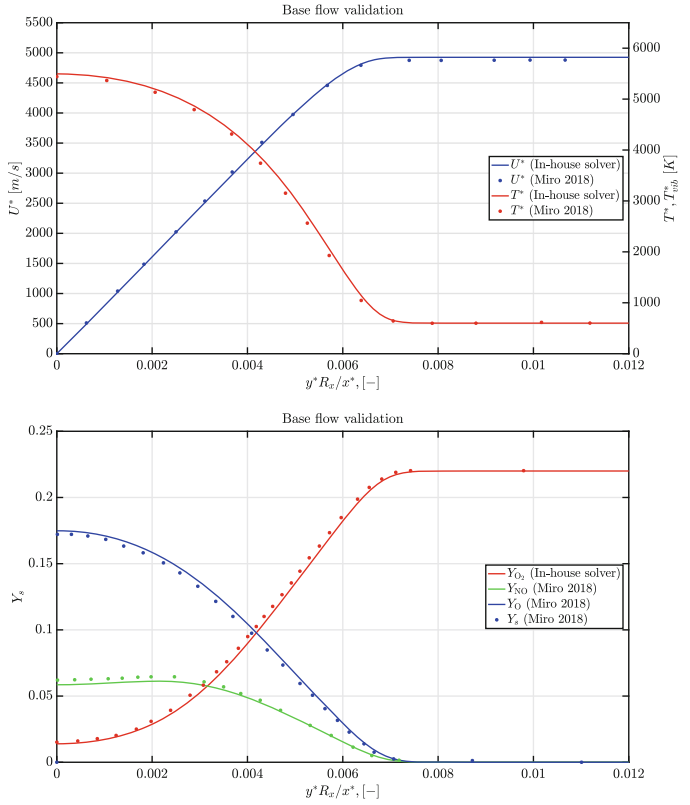

Fig. 2. Dimensional velocity, temperature and species profile over the wall-normal coordinate: comparison between the in-house base flow solver and Miró's results in [19].

– CNEQ case in [19]: The highly reacting flat plate flow is investigated. Air is modeled as mixture of 78% N_2 and 22% O_2. The flow is in chemical non-equilibrium with a Mach number of 10 and unit Reynolds number is 6.6×10^6/m. The free stream temperature is set to 600 K and the wall is adiabatic.

The dimensional velocity, temperature and species profiles are extracted at $x^* = 0.6$ m. The results are plotted in Fig. 2. The chemical equilibrium constants used in this paper are taken from the Park's curves fit, and are different from the literature so the results are generally fitted but slightly different.

3 Linear Stability Analysis

In order to investigate the stability of the flat plate flow, the modal stability analysis is introduced. This means, one focuses on the development of unstable eigenmodes (exponential growing disturbances) inside the flow field.

3.1 Linear Stability Equations

The linear stability analysis is based on the compressible Navier-Stokes equations in Sect. 2. All flow variables are split into a steady and a fluctuation part:

$$\boldsymbol{q}(x, y, z, t) = \bar{\boldsymbol{q}}(x, y) + \boldsymbol{q}'(x, y, z, t) \tag{6}$$

The steady state is a solution of the 2-D base flow in Sect. 2, whereas the fluctuation variable vector remains unsteady and 3-D:

$$\bar{\boldsymbol{q}}(x, y) = (\bar{\rho}, \bar{u}, \bar{v}, \bar{w}, \bar{T}, \bar{Y}_s, \bar{T}_{vib})$$

$$\boldsymbol{q}'(x, y, z, t) = \left(\rho', u', v', w', T', Y_s', T_{vib}'\right)$$

Once the flow variables in the NS equations are replaced by Eq. 6, the base flow is subtracted and the resulting linearized equations are written as:

$$\begin{aligned} \boldsymbol{\Gamma}\frac{\partial \boldsymbol{q}'}{\partial t} + \boldsymbol{A}\frac{\partial \boldsymbol{q}'}{\partial x} + \boldsymbol{B}\frac{\partial \boldsymbol{q}'}{\partial y} + \boldsymbol{C}\frac{\partial \boldsymbol{q}'}{\partial z} + \boldsymbol{D}\boldsymbol{q}' \\ = \boldsymbol{H}_{xx}\frac{\partial^2 \boldsymbol{q}'}{\partial x^2} + \boldsymbol{H}_{yy}\frac{\partial^2 \boldsymbol{q}'}{\partial y^2} + \boldsymbol{H}_{zz}\frac{\partial^2 \boldsymbol{q}'}{\partial z^2} + \boldsymbol{H}_{xy}\frac{\partial^2 \boldsymbol{q}'}{\partial x \partial y} + \boldsymbol{H}_{yz}\frac{\partial^2 \boldsymbol{q}'}{\partial y \partial z} + \boldsymbol{H}_{xz}\frac{\partial^2 \boldsymbol{q}'}{\partial x \partial z} \end{aligned} \tag{7}$$

where matrices $\boldsymbol{\Gamma}$, $\boldsymbol{A}$, $\boldsymbol{B}$, $\boldsymbol{C}$, $\boldsymbol{D}$, $\boldsymbol{H}_{xx}$, $\boldsymbol{H}_{yy}$, $\boldsymbol{H}_{zz}$, $\boldsymbol{H}_{xy}$, $\boldsymbol{H}_{yz}$, $\boldsymbol{H}_{xz}$ are 10×10 matrices and function of the mean flow variables. The resulting linear stability equations are valid for any kind of flow. As the following research deals with a flat plate boundary layer, a further simplification, i.e. "locally parallel flow", can be undertaken similarly to [5, 18], which leads to:

$$\bar{v} = 0, \ \frac{\partial \bar{\boldsymbol{q}}}{\partial x} = 0, \ \frac{\partial \bar{\boldsymbol{q}}}{\partial z} = 0$$

meaning that it is the local boundary-layer profile determining the flow instability. The last step is to apply a modal ansatz for the disturbances, this can be written in a wave-like form:

$$\boldsymbol{q}' = \boldsymbol{q}'(x, y, z, t) = \tilde{\boldsymbol{q}}(y) \exp[\mathrm{i}(\alpha x + \beta z - \omega t)] + \text{c.c.} \tag{8}$$

with $\mathrm{i}^2 = -1$ and c.c. denotes the complex conjugate. Parameters α, β and ω are the stream-wise, span-wise and time-wise wave numbers. Spatial theory is chosen over the temporal theory so that the disturbance waves are periodic in t and z growing in x, thus α is a complex number and whereas ω and β are real:

$$\alpha = \alpha_r + \mathrm{i}\alpha_i, \omega = \omega_r, \beta = \beta_r$$

In this research we focus only on 2-D disturbances so $\beta = 0$. The behaviour of small disturbances depends on the term $\exp(-\alpha_\mathrm{i} \mathrm{x})$; as x is always positive (streamwise direction), growth takes place for $\alpha_\mathrm{i} < 0$.

Once Eq. 8 is inserted in the linear stability equations the resulting modal system constitutes an Eigenvalue Problem (EP). Eigenvalues and eigenvectors can be obtained through two different methods:

- global method (GM): the modal system is rewritten into large matrices and discretized. The EP is solved by a standard eigenvalue solver and both discrete and continuous modes can be obtained.
- local method (LM): a close initial eigenvalue guess is needed (e.g. from the GM), then the correct eigenvalue is computed using iterative methods. Only one eigenvalue near the guess can be obtained, but this is fast and accurate.

3.2 Global Method

After introducing Eq. 8, linear stability equations can be written in a compact matrix form resulting into a non-linear EP of second order:

$$\boldsymbol{R}\tilde{\boldsymbol{q}} + \boldsymbol{S}\frac{\mathrm{d}\tilde{\boldsymbol{q}}}{\mathrm{d}y} + \boldsymbol{T}\frac{\mathrm{d}^2\tilde{\boldsymbol{q}}}{\mathrm{d}y^2} = \alpha\left(\boldsymbol{M}\tilde{\boldsymbol{q}} + \boldsymbol{N}\frac{\mathrm{d}\tilde{\boldsymbol{q}}}{\mathrm{d}y}\right) + \alpha^2\boldsymbol{P}\tilde{\boldsymbol{q}} \tag{9}$$

In order to solve Eq. 9 a spectral method with Chebyshev collocation points is used here. The method is easy to implement and performs best for high speed flows where eigenvalues lie close to each other [17]. The new transformed EP derived from Eq. 9 is:

$$\begin{bmatrix} \boldsymbol{R}' + \boldsymbol{S}'\boldsymbol{D}_n + \boldsymbol{T}'\boldsymbol{D}_n^2 & \mathbf{0} \\ \mathbf{0} & \mathbf{I} \end{bmatrix} \begin{bmatrix} \tilde{\boldsymbol{Q}} \\ \alpha\tilde{\boldsymbol{Q}} \end{bmatrix} = \alpha \begin{bmatrix} \boldsymbol{M}' + \boldsymbol{N}'\boldsymbol{D}_n & \boldsymbol{P} \\ \mathbf{I} & \mathbf{0} \end{bmatrix} \begin{bmatrix} \tilde{\boldsymbol{Q}} \\ \alpha\tilde{\boldsymbol{Q}} \end{bmatrix} \tag{10}$$

with the global vector of disturbances as $\tilde{Q} = \left(\tilde{q}_1, \tilde{q}_2, \cdots, \tilde{q}_j, \cdots, \tilde{q}_N\right)$ and the Chebyshev differentiation matrix as D_n. Matrices $\boldsymbol{R}'$, $\boldsymbol{S}'$, $\boldsymbol{T}'$, $\boldsymbol{M}'$, $\boldsymbol{N}'$, $\boldsymbol{P}'$ are a function of the namesake matrices in Eq. 9.

Boundary conditions for Eq. 10 need to be prescribed at both ends of the computational domain. At the wall:

$$y = 0\text{: } \tilde{u} = \tilde{v} = \tilde{w} = \tilde{T} = \tilde{T}_{vib} = \frac{\mathrm{d}\tilde{Y}_s}{\mathrm{d}y} = 0 \tag{11}$$

In the freestream:

$$y \to \infty\text{: } \tilde{u} = \tilde{v} = \tilde{w} = \tilde{T} = \tilde{T}_{vib} = \tilde{Y}_s = 0 \tag{12}$$

Equation 12 is just an approximation of the disturbances in the free stream; in reality, the perturbations in the free stream are not exact zero. One can extend the mesh to a value much greater than the boundary layer thickness, this is instead computationally inefficient and physically incorrect. Instead of the GM, the local method can be applied.

3.3 Local Method

In the LM it is preferable to reduce the order of the system in Eq. 9 to a first order EP as:

$$\frac{\mathrm{d}\tilde{\boldsymbol{q}}}{\mathrm{d}y} = \boldsymbol{L}\tilde{\boldsymbol{q}} \tag{13}$$

where L is a 18 × 18 matrix obtained from the linear stability equations and $\mathrm{q}\sim$ is the new disturbance vector containing also first order derivatives as:

$$\tilde{\boldsymbol{q}} = \left(\tilde{\rho}, \tilde{u}, \tilde{v}, \tilde{w}, \tilde{T}, \tilde{Y}_s, \tilde{T}_{vib}, \frac{\mathrm{d}\tilde{u}}{\mathrm{d}y}, \frac{\mathrm{d}\tilde{w}}{\mathrm{d}y}, \frac{\mathrm{d}\tilde{T}}{\mathrm{d}y}, \frac{\mathrm{d}\tilde{Y}_s}{\mathrm{d}y}, \frac{\mathrm{d}\tilde{T}_{vib}}{\mathrm{d}y}\right)$$

Different from the GM, the LM applies a non-zero BC in the freestream:

$$y \to \infty\text{: } \tilde{u} = \tilde{v} = \tilde{w} = \tilde{T} = \frac{\mathrm{d}\tilde{Y}_s}{\mathrm{d}y} = \tilde{T}_{vib} < \infty \tag{14}$$

The solution of LM is obtained by integrating Eq. 13 from the free stream to the wall using a Runge Kutta 4-th order method. The solution of is a linear combination of fundamental solutions $\varphi_k(y)$ as:

$$\tilde{\boldsymbol{q}}(y) = \sum_k C_k \boldsymbol{\varphi}_k(y) \tag{15}$$

where C_k are linear combination coefficients calculated through the boundary conditions at the wall. In the free stream the fundamental solutions have the simple form of:

$$\boldsymbol{\varphi}_{\infty,k}(y) = \boldsymbol{v}_{\infty,k} \exp\left(\lambda_{\infty,k} y\right) \tag{16}$$

as in case of the flat plate, the matrix $\boldsymbol{L}$ is constant for $y \to \infty$. The eigenvalue search is done iteratively using the temperature disturbance at the wall ($\tilde{T}(0)$) as iteration criterion. Over each iteration the searched eigenvalue α is calculated through the secant method as:

$$\alpha^{n+1} = \alpha^n - \tilde{T}^n(0) \frac{\alpha^n - \alpha^{n-1}}{\tilde{T}^n(0) - \tilde{T}^{n-1}(0)} \tag{17}$$

where n is the iteration number and α_0 is obtained from the GM.

3.4 Verification

Validation of the stability solver is performed with a comparison to the latest literature sources available. The in-house stability solver has been verified against two different kind of flows, a TNEQ and CNEQ case.

– TNEQ case in [18]: The instability of a highly cooled flat plate flow is investigated. The flow is in thermal non-equilibrium with a Mach number of 4.5 and free stream pressure of 10 kPa. The free stream temperature is set to 1500 K and isothermal wall at 300 K is prescribed. The instability analysis is carried out at $Re_x = 2000$ with a special analysis of the dispersion curve. Spatial growth rate $-\alpha_i$ and real phase speed c_r are calculated at different frequencies. The LM, combined with the GM as initial value, is used with $N = 1000$ grid points in wall-normal distance. The results are plotted in Fig. 3.

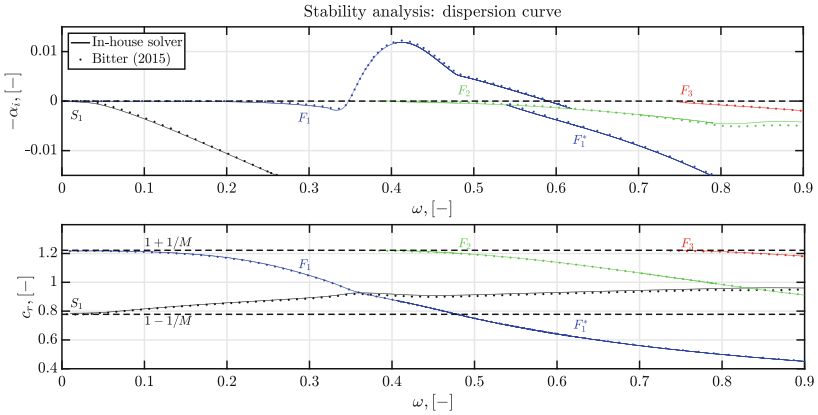

Fig. 3. Dimensionless spatial growth rate (top figure) and real phase speed (bottom figure) over the frequency: comparison between the in-house stability solver and Bitter's results [18]. The stability solver shows good agreement with the literature results.

Wall cooling destabilizes the fast mode F_1 and stabilizes the slow mode S_1. A new supersonic mode F_1^* arises through the synchronization of F_1 with the continuous spectrum. For further information, see the work of [18].

– CNEQ case in [19]: The instability of a highly reacting flat plate flow is investigated. The flow condition is exactly the same case as the verification of the base flow. The results are plotted in Fig. 4 and the growth rate of the S_1 mode fits well.

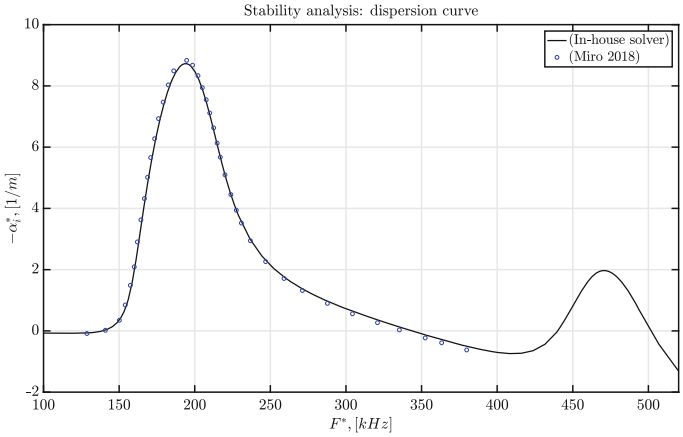

Fig. 4. Dimensional spatial growth rate over the frequency: comparison between the in-house stability solver and Miró's results in [19]

4 Results

The new supersonic mode F_1^*, introduced in Sect. 3, is analyzed more in detail. Modal stability analysis is able to capture this unique feature of the second mode as it gets unstable and travels supersonically with respect to the free stream. This means that oscillatory disturbance waves are travelling outside the boundary layer and are not decaying the free stream. Indeed, as one can see from Fig. 5 the global method is not able to capture this phenomenon and fails to converge.

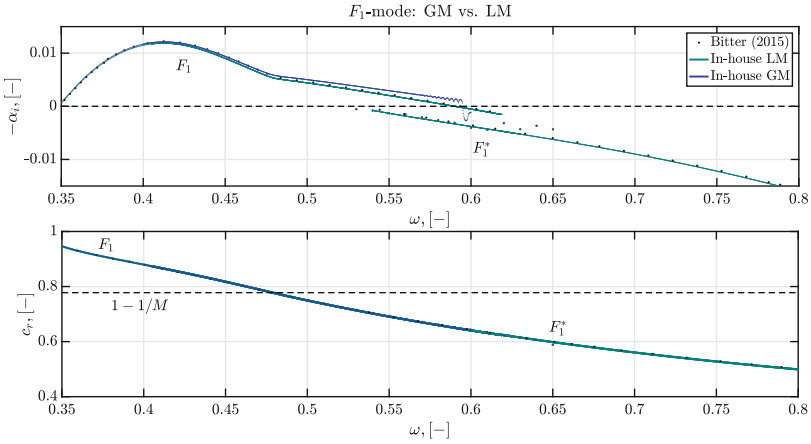

Fig. 5. Dimensionless spatial growth rate (top figure) and real phase speed (bottom figure) over the frequency: comparison between the global and local method solver

The problem of the global method lies in its free stream boundary conditions (Sect. 3). Local method bounds the BCs to a finite value, thus the supersonic mode is well captured similarly to [18]. Not only the F_1^* mode is of interest, in highly cooled walls the modal instability is due to the F_1 mode. In the following analysis, effects of the Reynolds number (Re_x) and the free stream/wall temperature (T_∞^*, T_w^*) are evaluated. Moreover, two different kind of hypersonic flows are considered, a CPG flow and a TNEQ flow. The flow parameters are the same as in Sect. 2.3.

- Reynolds number: the modal stability analysis is carried out at two different local Reynolds numbers ($Re_x = 500$, 2000). Results of the unstable F_1^- mode are shown in Fig. 6.

First of all, one can notice the effect of TNEQ on the growth rate. Vibrational non-equilibrium causes a destabilization of the F_1 mode. However, this is dependent on the local Reynolds number. At low Reynolds numbers the flow is still frozen and energy exchange between translational and vibrational energy modes is not yet activated. At higher Re_x the flow is in non-equilibrium. This behaviour can be explained by taking the vibrational source term in the dimensionless boundary layer equations $Re_\xi Q_{t-v}$. Energy exchange takes place only when Re_L is big enough.

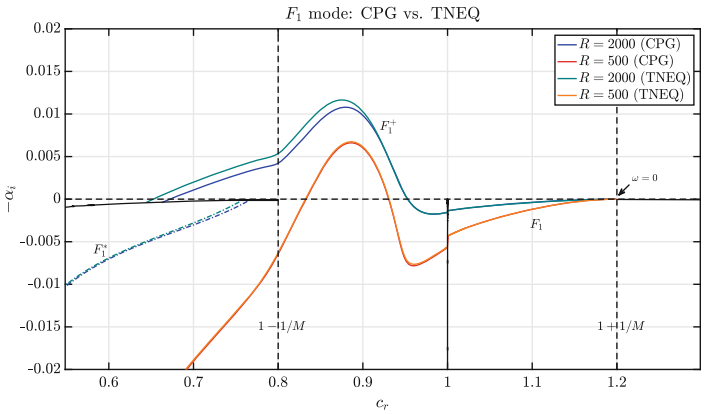

Fig. 6. Spatial growth rate over the real phase speed for the F_1^- mode: comparison between CPG and TNEQ flows with ($Re_x = 500, 2000$)

Moreover, at low Reynolds numbers the F_1 mode becomes stable before the slow acoustic branch point ($\alpha_i = 0$, $c_r = 0.8$). No supersonic mode is observed. At high Re_x the F_1 mode shows a kink, this is due to its synchronization with the slow acoustic waves ($c_r = 0.8$). With a certain phase speed delay, a new discrete but stable mode F_1^* is generated, however the starting point and the slopes coincide for both CPG and TNEQ flows.

Last but not least, the synchronization of the F_1^* mode with the entropy/vorticity spectrum at $c_r = 1$ reveals a Re_x dependence. At lower Re_x, due to the interaction with the S_1 mode (here not displayed), the dampening appears to be stronger than for the $Re_x = 2000$ mode. Overall, further analyses need to be undertaken.

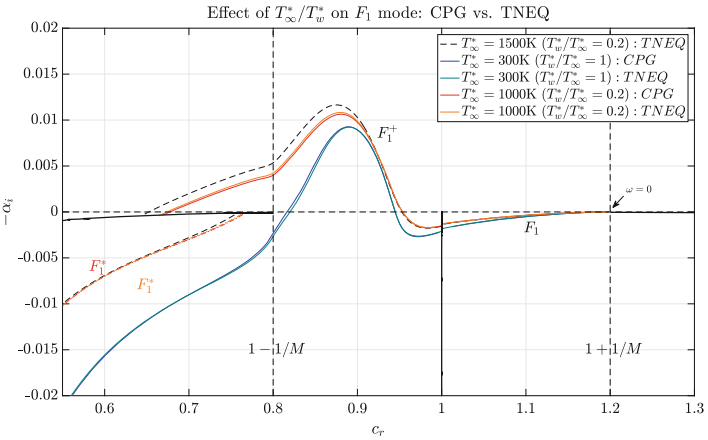

Fig. 7. Spatial growth rate over the real phase speed for the F_1 mode: comparison between CPG and TNEQ flows with $T_w^*/T_\infty^* = 0.2$ and T_∞^* = 300 K, 1000 K, 1500 K

- Wall and free stream temperatures (T^*_∞, T^*_w): the modal stability analysis is carried out at two different T^*_w/T^*_∞ ratios $(0.2, 1)$ with three different free stream temperatures T^*_∞ (300 K, 1000 K, 1500 K). Results of the unstable F_1 mode are shown in Fig. 7.

First of all, the supersonic mode F_1^* seems not affected by the variation of the free stream temperature. When the ratio T^*_w/T^*_∞ is kept constant, the mode coincides for T^*_∞ = 1000 K and T^*_∞ = 1500 K.

Furthermore, TNEQ has no influence on the supersonic mode but only on the F_1^+ mode; the variation, however, is small when T^*_∞ is low since the free stream temperature stands for the level of TNEQ in the flow. What alters significantly the second mode instability peak is the wall cooling, or better to say the ratio T^*_w/T^*_∞. This overwhelms the TNEQ effect for $T^*_w/T^*_\infty \ll 1$. Last but not least, the synchronization "jump" at $c_r = 1$ appears to be stronger at lower T^*_∞, meaning a greater dampening of the F_1 mode.

5 Conclusions

A boundary layer and modal stability solver have been developed and verified through literature comparisons for a hypersonic flat plate flow with high-temperature effects. The in-house solver shows good consistency both with base flow profiles and spatial growth rates for both TNEQ and CNEQ. New modal stability analyses for a TNEQ flow have been performed varying the Reynolds numbers, free stream temperature and wall temperature. At low Reynolds number the flow is still frozen. Both thermal non-equilibrium and wall cooling destabilize the second mode instability in different manners. TNEQ is only relevant at high-temperatures, where as wall cooling influences the modal growth already at low temperatures. The supersonic mode is not influenced by the TNEQ. Future steps include the further analysis of the aforementioned parameters with special focus on the disturbance eigen-functions and LST N-factors. Moreover, thermal and chemical equilibrium is under investigation. Last but not least, other gases need to be considered such as oxygen and its high disturbance dampening feature.

References

1. Morkovin V, Reshotko E, Herbert T (1994) Transition in open flow systems – a reassessment. Bull Am Phys Soc 39:1882
2. Reed HL, Saric WS, Arnal D (1996) Linear stability theory applied to boundary layers. Annu Rev Fluid Mech 28(1):389–428
3. Anderson JD (2006) Hypersonic and high-temperature gas dynamics, 2nd edn. McGraw Hill, New York
4. Gnoffo PA, Gupta RN, Shinn JL (1989) Conservation equations and physical models for hypersonic air flows in thermal and chemical nonequilibrium. NASA Technical Paper No. 2867

5. Malik MR, Anderson EC (1991) Real gas effects on hypersonic boundary-layer stability. Phys Fluids A 3(5):803–821
6. Stuckert G, Reed HL (1994) Linear disturbances in hypersonic, chemically reacting shock layers. AIAA J 32(7):1384–1393
7. Hudson M, Chokani N, Candler G (1997) Linear stability of hypersonic flow in thermo-chemical nonequilibrium. AIAA J 35(35):958–964
8. Klentzman J, Tumin A (2013) Stability and receptivity of high speed boundary layers in oxygen. In: Fluid dynamics and co-located conferences. American Institute of Aeronautics and Astronautics
9. Fedorov A, Tumin A (2012) High-speed boundary-layer instability: old terminology and a new framework. AIAA J 49(8):1647–1657
10. Millikan RC, White DR (1963) Systematics of vibrational relaxation. J Chem Phys 39 (12):3209–3213
11. Park C, Jae RL, Partridge H (2001) Chemical-kinetic parameters of hyperbolic earth entry. J Thermophys Heat Transfer 15(1):76–90
12. Park C (1987) Assessment of two-temperature kinetic model for ionizing air. J Thermophys Heat Transfer 3(3):233–244
13. Wilke CR (1950) A viscosity equation for gas mixtures. J Chem Phys 18(4):517–519
14. Blottner FG, Johnson M, Ellis M (1971) Chemically reacting viscous ow program for multi-component gas mixtures. Technical report, Sandia Labs., Albuquerque
15. Vincenti WG, Kruger CH (1965) Introduction to physical gas dynamics. Wiley, New York
16. Prakash A, Parsons N, Wang X, Zhong X (2011) High-order shock-fitting methods for direct numerical simulation of hypersonic flow with chemical and thermal nonequilibrium. J Comput Phys 230(23):8474–8507
17. Pinna F (2012) Numerical study of stability of flows from low to high Mach number. PhD Thesis, von Karman Institute for Fluid Dynamics and Universita La Sapienza di Roma
18. Bitter NP (2015) Stability of hypervelocity boundary layers. PhD Thesis, California Institute of Technology, California
19. Miró FM (2018) Diffusion and chemical non-equilibrium effects on hypersonic boundary-layer stability. In: AIAA aerospace sciences meeting